

In Situ Neutron Diffraction Analyzing Stress-Induced Phase Transformation and Martensite Elasticity in [001]-Oriented $\text{Co}_{49}\text{Ni}_{21}\text{Ga}_{30}$ Shape Memory Alloy Single Crystals

A. Reul¹ · C. Lauhoff² · P. Krooß² · M. J. Gutmann³ · P. M. Kadletz¹ ·
Y. I. Chumlyakov⁴ · T. Niendorf² · W. W. Schmahl¹

Published online: 26 February 2018
© ASM International 2018

Abstract Recent studies demonstrated excellent pseudoelastic behavior and cyclic stability under compressive loads in [001]-oriented Co–Ni–Ga high-temperature shape memory alloys (HT-SMAs). A narrow stress hysteresis was related to suppression of detwinning at RT and low defect formation during phase transformation due to the absence of a favorable slip system. Eventually, this behavior makes Co–Ni–Ga HT-SMAs promising candidates for several industrial applications. However, deformation behavior of Co–Ni–Ga has only been studied in the range of theoretical transformation strain in depth so far. Thus, the current study focuses not only on the activity of elementary deformation mechanisms in the pseudoelastic regime up to maximum theoretical transformation strains but far beyond. It is shown that the martensite phase is able to withstand about 5% elastic strain, which significantly increases the overall deformation capability of this alloy system. In situ neutron diffraction experiments were carried out using a newly installed testing setup on Co–Ni–Ga single crystals in order to reveal the nature of the stress–strain response seen in the deformation curves up to 10% macroscopic strain.

Keywords Shape memory alloy (SMA) · Martensitic phase transformation · In situ neutron diffraction · Martensite stabilization · Pseudoelasticity

Introduction

High-temperature shape memory alloys (HT-SMAs) received increasing attention over the last decades due to numerous potential applications within various fields [1–3]. Their unique functional properties are based on a fully reversible thermoelastic phase transformation from a high-temperature austenitic phase to a low-temperature martensitic phase [1, 2, 4]. Due to their large recoverable strains, HT-SMAs are promising candidates for applications as solid-state actuators or damping devices to be employed at elevated temperatures [3, 5]. Particularly in the automotive and aerospace sectors, operating temperatures can be often above 100 °C. Conventional binary Ni–Ti SMAs exhibit fully reversible transformation at temperatures only up to about 100 °C, and suffer from microstructural instability due to uncontrollable precipitation of secondary phases at higher temperatures and the activation of slip [3, 4]. In recent years, several new alloy systems were introduced in order to increase martensite start temperatures (M_s) and reversible transformation strains beyond values reported for binary Ni–Ti. The substitution of Ti in Ni–Ti by Hf or Zr and Ni by Pd or Pt enabled the increase of M_s in ternary Ni–Ti–(Hf, Zr) and Ni–Ti–(Pd, Pt) considerably [3, 4, 6]. However, high costs of Pd and Pt and limited formability of Ni–Ti–(Hf, Zr) alloys featuring high transformation temperatures limit a widespread application of these ternary alloys so far, even if current findings for Ni–Ti–Hf alloys are very promising [7, 8]. Beside ternary Ni–Ti–X HT-SMAs, low-cost Cu–

✉ T. Niendorf
niendorf@uni-kassel.de

¹ Applied Crystallography, Department of Earth and Environmental Sciences, Ludwig-Maximilians-Universität, 80333 Munich, Germany

² Institute of Materials Engineering, University of Kassel, 34125 Kassel, Germany

³ ISIS Facility, Rutherford Appleton Laboratory, Chilton Didcot, Oxfordshire OX11 0QX, UK

⁴ Siberian Physical Technical Institute, Tomsk State University, Novosobornay Square 1, 634050 Tomsk, Russia

based alloys were identified as competitive SMAs for high-temperature applications. Ternary Cu–Al–Ni alloys offer pseudoelastic strains of up to 17%, however, suffer from microstructural instability at high temperatures [1, 4]. In this regard, the Heusler-type Co–Ni–Ga alloys are attractive alternatives due to excellent functional properties, even at high temperatures up to 500 °C. Due to relatively inexpensive constituents Co–Ni–(Al, Ga) and good workability as a result of the potential precipitation of the ductile Co-rich γ -phase (fcc), major roadblocks towards application can be overcome. Furthermore, widely tunable transformation temperatures (–150 to 200 °C) as well as a wide temperature range for pseudoelasticity (RT to 500 °C) make Co–Ni–Ga very promising for high-temperature smart applications [4, 9–11].

Recent studies [11–13] focusing on as-grown [001]-oriented $\text{Co}_{49}\text{Ni}_{21}\text{Ga}_{30}$ single crystals in compression revealed a fully pseudoelastic response up to 500 °C in single cycle experiments up to maximum transformation strains. However, various microstructural mechanisms contributing to martensite stabilization were already identified, either in cyclic experiments or after long-term thermal exposure [11, 14–18]. One potential detrimental effect is the pinning of moving martensite interfaces by point defects which is more pronounced at elevated temperatures leading to self-accommodated martensite with multivariant microstructure [19]. Another important mechanism is the detwinning of martensite which necessitates the nucleation of new habit planes between austenite and detwinned martensite for the onset of the reverse transformation [16]. In [11, 12, 20], excellent pseudoelastic behavior and cyclic stability in [001]-oriented single crystalline Co–Ni–Ga alloys were demonstrated under compression at room temperature. One important aspect in this regard is the suppression of dislocation slip in austenite in the $\{110\} \langle 001 \rangle$ slip system. Maximum theoretical transformation strains of 4.8 and 8.6% in compression and tension, respectively, were calculated for [001]-oriented single crystals using the energy minimization theory [20, 21]. A narrow stress hysteresis and a high resistance to material degradation point out the great potential of Co–Ni–Ga SMAs in numerous applications.

However, all studies available in open literature so far focus on the thermo-mechanical behavior and functional stability of Co–Ni–Ga only up to maximum theoretical transformation strains. Potential extension of the pseudoelastic strain capability by exploration of the elastic martensite deformation has not been addressed so far. Thus, the focus of this study is the characterization of prevalent deformation mechanisms upon elastic deformation of martensite in a [001]-oriented $\text{Co}_{49}\text{Ni}_{21}\text{Ga}_{30}$ single crystal under compression at high stress levels up to about 1000 MPa. Besides dislocation activity or detwinning,

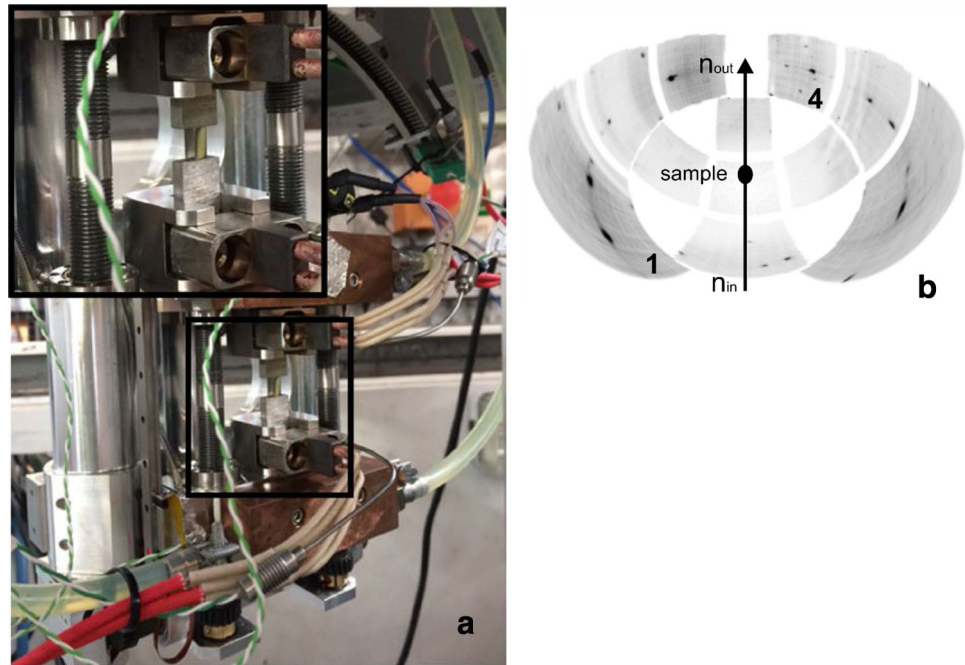
additional twinning modes could be expected at high prevailing stresses to accommodate the applied deformation. In this regard, in situ neutron diffraction is an appropriate experimental technique for the evaluation of twinning under applied stress as pointed out by Molnár et al. [22]. In their study, the authors demonstrated the differentiation of individual stress-induced martensite variants in Cu–Al–Ni single crystals during compressive loading. Furthermore, it has been proven that neutron diffraction is a valuable method for phase quantification providing structural information from bulk specimens [11, 22–25]. Thus, for in-depth analysis of elementary deformation mechanisms in Co–Ni–Ga under the conditions detailed above a newly installed experimental setup at the ISIS neutron source has been employed for the first time.

Materials and Experimental Techniques

A large single crystal with a nominal composition of $\text{Co}_{49}\text{Ni}_{21}\text{Ga}_{30}$ was grown using the Bridgeman technique in a He environment. $3 \times 3 \times 6 \text{ mm}^3$ as-grown compression specimens were obtained by electro-discharge machining (EDM) from the bulk single crystal such that the longer load axes were parallel to the [001]-direction of the austenitic phase. Finally, samples were mechanically ground in order to remove the EDM affected surface layer.

In situ neutron diffraction was carried out using the single-crystal diffractometer SXD at the ISIS neutron source, Rutherford Appleton Laboratory, Oxfordshire. The as-grown specimen was compressed at room temperature in an uniaxial single cycle experiment using a newly installed miniature load frame (Kammrath und Weiss, Germany) capable of $\pm 10 \text{ kN}$ in displacement control at a nominal displacement rate of $5 \times 10^{-3} \text{ mms}^{-1}$ with a maximum load of 1030 MPa upon loading and a given minimum stress after unloading (Fig. 1a). Strains were calculated from displacement data. Reflections from the 002 and 200 lattice planes of austenite were centered on high-angle detector 1 and low-angle detector 4 of SXD by a rotation of the sample around its vertical axis to a fixed position of 26° (Fig. 1b). As is highlighted in the corresponding figure caption, the load frame installed shades the detectors below the sample. However, initial alignment of the sample allowed for evaluation of deformation response of the [001]-oriented Co–Ni–Ga single crystal, which is characterized by a phase transformation from the partially ordered B2 austenite [23] to the partially ordered L1_0 martensite phase. Obviously, the shading of the detector array below the sample reduces the number of accessible diffraction peaks. However, it has no detrimental effect on the quality of data in this experiment, since Laue time-of flight Technique enables the complete determination of the

Fig. 1 **a** Newly installed miniature loadframe and **b** detector arrangement of SXD. Data were analyzed on high-angle detector 1 and low-angle detector 4. The load frame shades the detectors below the sample



lattice and phase state of the alloy. For further details on the setup of SXD, the reader is referred to [26]. Diffraction data were recorded on six equatorial detectors for 60 min during each loading stage, three in the austenite elastic region, four on the stress–strain plateau and eleven in the martensite elastic region. Four detectors at an angle of 45° to the equatorial plane and one directly beneath the sample were not accessible in this experiment due to shading by the miniature load frame.

SXD uses the neutron time-of-flight technique to acquire diffraction data of a single crystalline specimen at a fixed orientation 2Θ . A polychromatic neutron beam, covering wavelengths in a range of $0.2\text{--}10\text{ \AA}$, is scattered on the single-crystal specimen. Scattered neutrons are collected as a function of time-of-flight on eleven large area two-dimensional LiF/ZnS position-sensitive detectors (PSDs) arranged around the sample position. This setup allows to cover diffraction data within a wide range of reciprocal space increasing the speed of data collection compared to monochromatic single-crystal neutron diffractometers [26]. Diffraction data collected on high-angle detector 1 and low-angle detector 4 were indexed and integrated using the software package SXD2001 in the current work [26].

Results

Figure 2 presents the results of a pseudoelastic uniaxial single cycle compression experiment at room temperature of the as-grown $[001]$ -oriented $\text{Co}_{49}\text{Ni}_{21}\text{Ga}_{30}$ single crystal. Diffractograms were recorded at different stages during

loading and unloading. For the sake of brevity, diffraction data of eight out of 18 diffractograms collected on high-angle detector 1 are displayed in Fig. 2a–h; two in the elastic austenite region (region I, Fig. 2a, h), two on the pseudoelastic stress plateau (region II, Fig. 2b, g) and four in the elastic martensite region (region III, Fig. 2c–f). In region I, the specimen in its initial state is entirely austenitic (Fig. 2a). After the initial linear elastic austenite deformation, the stress-induced phase transformation from the partially ordered B2 austenite [23] to the partially ordered $L1_0$ martensite phase occurs gradually, which results in a constant stress plateau. In region II near the end of the stress plateau, the microstructure consists of almost 100% martensite. Here the corresponding diffractogram (Fig. 2b) shows a weak austenite (A) reflection between two strong martensite reflections (V_1 and V_2) at a total strain of about 4.3%. These two strong martensite reflections shown in Fig. 2b–g arise from the $(200)_{V_1}$ and $(002)_{V_2}$ lattice planes of two twin domain variants V_1 and V_2 , respectively. Correspondingly, at the end of the plateau, V_1 and V_2 form a simple regular twin structure. Space group and lattice parameters are Pm-3m (#221), $a = 2.879(2)\text{ \AA}$ for as-grown austenite and P4/mmm (#123), $a = 2.737(8)\text{ \AA}$, $c = 3.157(9)\text{ \AA}$ for stress-induced martensite (SIM). The inset in Fig. 2i sketches the formation of the two tetragonal martensite domain variants from B2 austenite under compressive load. As expected, their extensional c -axes are perpendicular to the $[001]$ compressive load direction and perpendicular to each other. Numerous additional observed reflections could be clearly assigned to various lattice planes of austenite in the initial

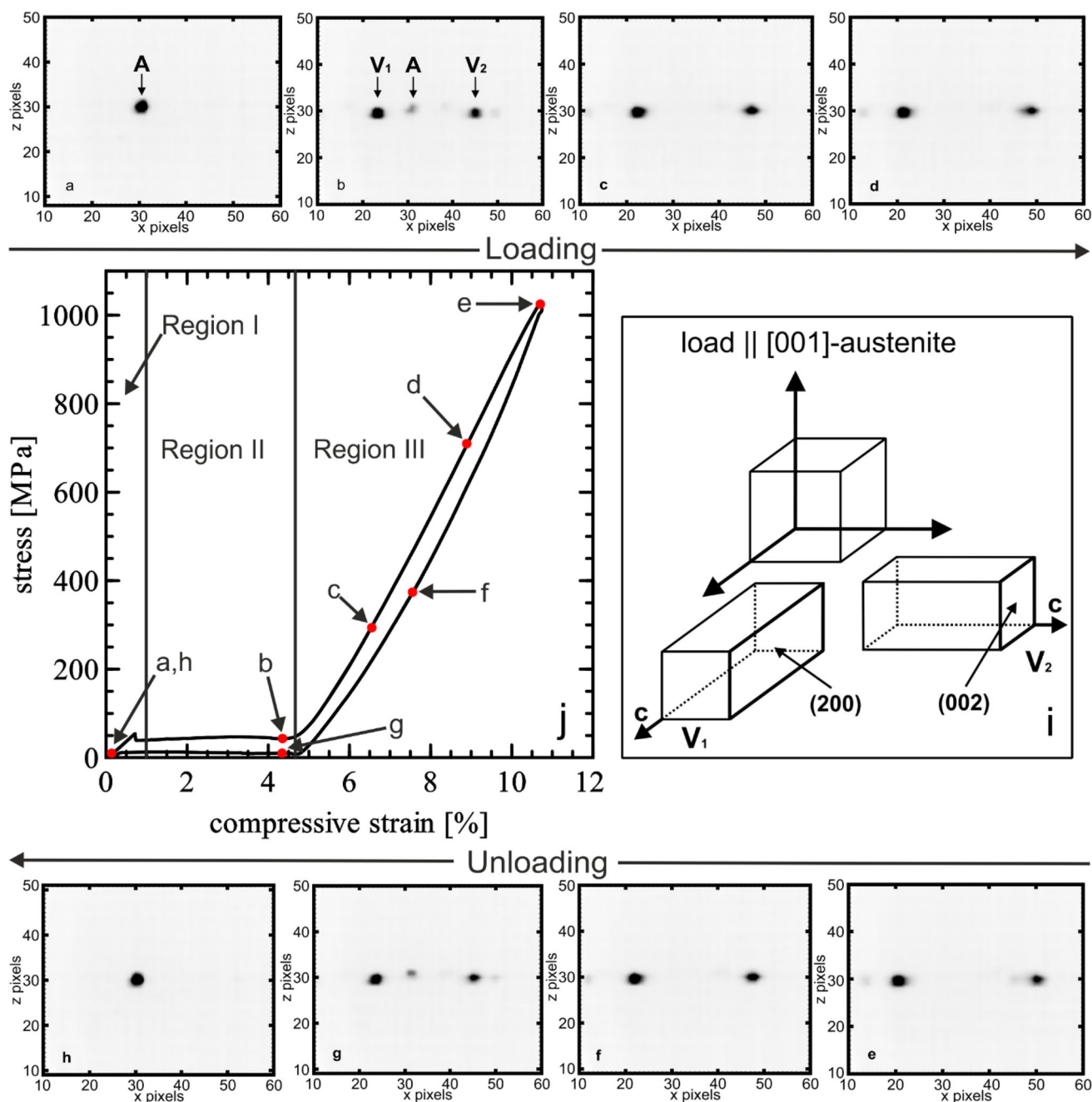


Fig. 2 Diffraction patterns of high angle detector 1 obtained from in situ neutron diffraction on [001]-oriented $\text{Co}_{49}\text{Ni}_{21}\text{Ga}_{30}$ under compression. The phase state and variant selection is marked for different regions: Elastic austenite region I, stress plateau region II and elastic

martensite region III. The inset (i) demonstrates the formation of the favorite two stress-induced martensite domain variants (V_1 and V_2) from bcc austenite (Color figure online)

stage (Fig. 3a, b) and martensite twin domain variants in the elastic martensite region (Fig. 3c, d).

Beyond the end of the stress-strain plateau at about 4.6% strain, where the stress-induced martensite transformation is completed, a further increase of stress is observed (Fig. 2j). The stress increase is due to elastic deformation of martensite (region III). The maximum strain achieved at 1030 MPa stress for the [001]-oriented Co–Ni–Ga single

crystal is 10.7% total strain in the current experiment, which includes phase transformation strain and elastic deformation (Fig. 2j, red dot highlighted “e”). Upon unloading from 1030 MPa in displacement control, a small hysteresis in stress for a given displacement in the elastic region in the martensite phase (Fig. 2j) is observed. Figure 4 displays the diffraction intensities as a function of macroscopic strain and demonstrates the formation of

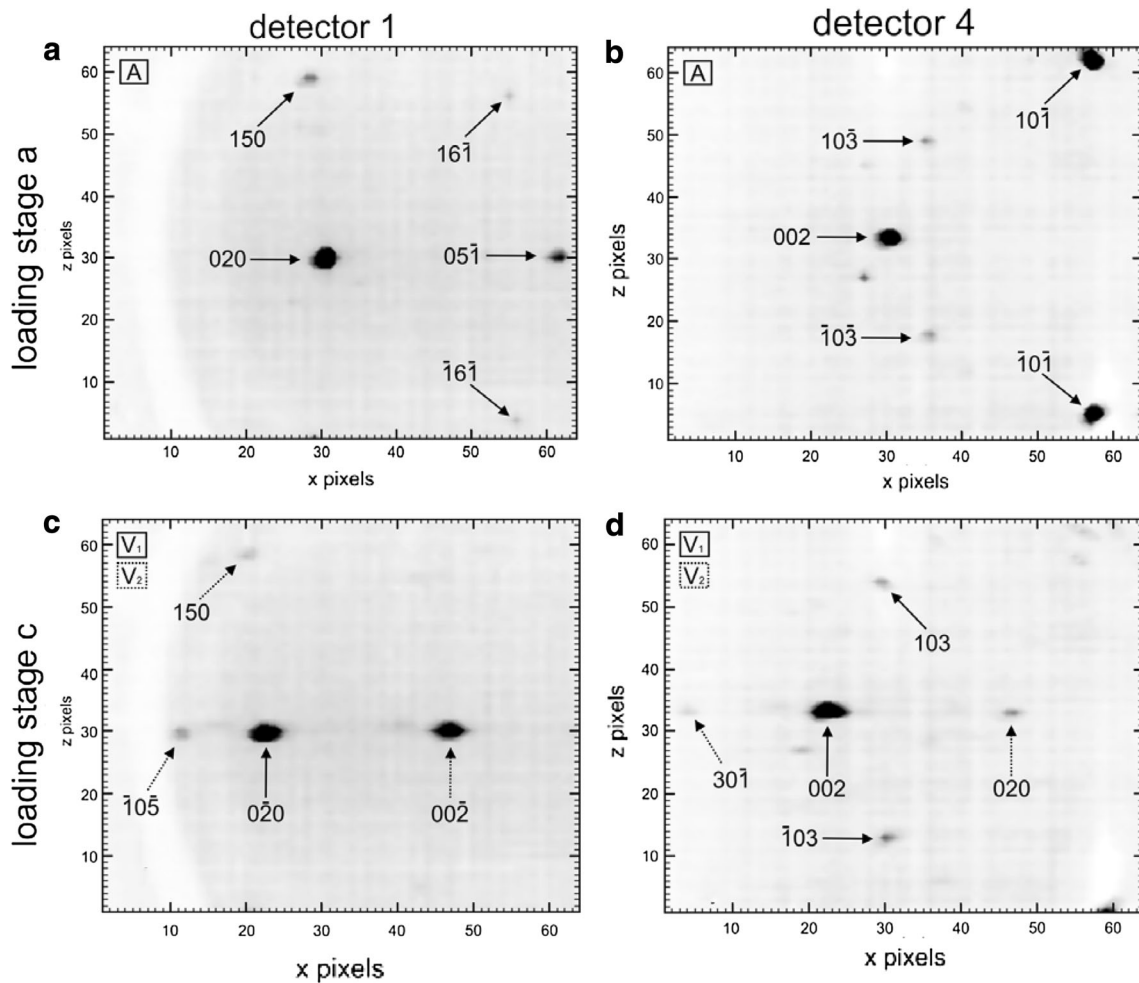
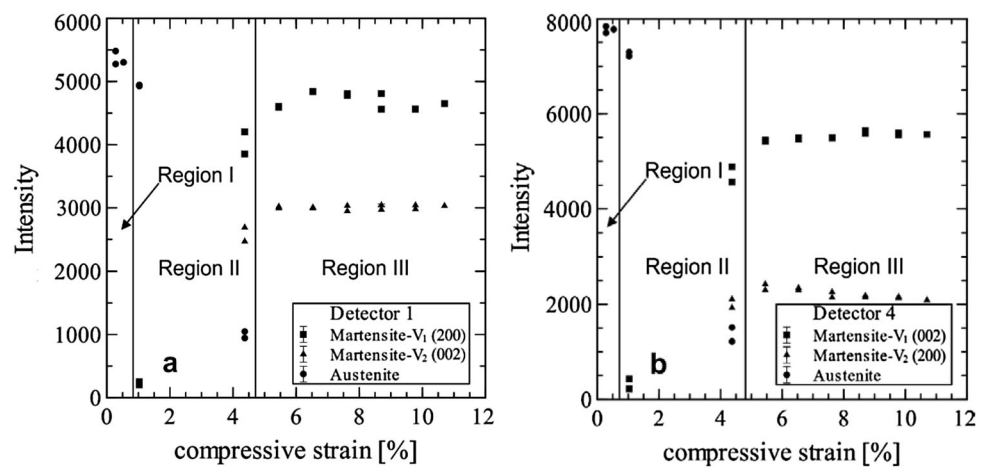


Fig. 3 Observed intensities on low- and high-angle detector 1 and 4; **a, b** intensities of austenite (A) without superimposed load; **c, d** intensities of two dominant stress-induced martensite domain

variants according to the schematic shown in Fig. 2i (V_1 and V_2) in the elastic martensite region. The formation of the third martensite domain variant is suppressed by the compressive stress along [001]

Fig. 4 Diffraction intensity plotted as a function of compressive strain. A higher intensity of V_1 during formation of stress-induced martensite (region II) demonstrates its favored growth with respect to V_2 . Constant intensities in region III reveal a constant volume fraction of both martensite domain variants



stress-induced martensite along the plateau (region II) during forward transformation and full recovery of austenite in the reverse transformation. A notable rise in

intensity of martensite V_1 is observed at a very early stage of deformation of about 1% strain, whereas the diffraction peak from martensite domain variant V_2 was observed only

at the end of the stress–strain plateau. As focus was on the elementary deformation mechanisms in region III in this study, only two diffractograms in the plateau region were measured and, thus, the onset of variant formation and successive growth was not determined in detail here. In region III, intensities of both martensite domain variants remain almost constant independent of the loading condition. This clearly indicates that the volume fraction of both martensite domain variants remains essentially constant upon loading and unloading in region III. An increase of the volume fraction of one of the martensite variants at the expense of the other one would have resulted in a change of their respective diffraction intensities. However, this was not observed during deformation in the elastic martensite region III up to strains of 10.7%.

The reverse transformation to austenite occurs at a constant plateau stress and its beginning is indicated by the formation of a weak austenite reflection between two strong martensite reflections at a total strain of 4.3% as marked in Fig. 2g. Finally, Fig. 2h reveals the austenite to be the dominant stable phase after unloading, indicating full strain recovery after a pseudoelastic deformation following one cycle up to highest stresses and strains as detailed before.

Discussion

In this study, in situ neutron diffraction was employed to reveal the evolution of phase state and martensite domain variants upon stress-induced martensite transformation of Co–Ni–Ga single crystals with an emphasis on the elastically strained martensite. For this, a newly installed testing setup at the SXD diffractometer was employed for the first time. The results obtained reveal a characteristic stress–strain response of Co–Ni–Ga single crystals in the [001]-orientation. As expected, the plateau region is characterized by the transition from initial austenite to stress-induced martensite upon loading of the sample. A similar transformation behavior of as-grown [001] oriented $\text{Co}_{49}\text{Ni}_{21}\text{Ga}_{30}$ single crystals in compression at room temperature was described in [13] and [20]; however, in these studies, single crystalline material was only deformed to the end of the stress–strain plateau, i.e., to about 4.3% strain. Furthermore, no microstructural information from the bulk material was provided. In situ high-spatial resolution optical microscopy characterization only was provided for the surface of the compression samples. The analysis of elementary mechanisms of deformation of a Co–Ni–Ga single crystal beyond the stress plateau and up to 10.7% strain provides new results broadening both the knowledge on and the application range of this HT-SMA. The initial formation of a single dominating variant of

stress-induced martensite followed by a plateau-type response with a maximum pseudoelastic strain of 4.3%, where the single martensite variant has become internally twinned, is in good agreement with the observations of [13, 20]. As already pointed out by [13], the width $\Delta\sigma$ of the stress hysteresis in [001]-oriented $\text{Co}_{49}\text{Ni}_{21}\text{Ga}_{30}$ is small as the potential generation of dislocations during compressive deformation at room temperature is hampered due to a lack of suitable slip systems. In the present experiment, it is observed that for the same reason the stress-induced martensite can be elastically deformed by another 6% strain beyond the plateau.

The Bain strain resulting from Pm-3m to P4/mmm martensite transformation elongates the tetragonal *c*-axis of the martensite and compresses the tetragonal *a*- and *b*-axis to provide for a volume strain close to zero, as required for shape memory behavior. Thus, in the compressive strain experiment with strain along $[001]_{\text{cubic}}$, the martensite domain variant V_3 with [001] martensite parallel to [001] cubic is suppressed, and only those two variants which have their *c*-axis perpendicular to the loading axis, V_1 and V_2 , are formed. Even at the beginning of region III (Fig. 3c, d), there is no evidence for the presence of the third domain variant. Moreover, from the two expected domain variants V_1 and V_2 , only one (labeled V_1) forms initially at the beginning of the stress-induced transformation; only at the end of the plateau, the presence of both variants V_1 and V_2 is observed (Fig. 4a, b). As the focus of the current study was on the characterization of region III, the onset of the formation of V_2 could not be precisely located on the stress plateau. This will be subject of future work. However, based on the experiments described by [13], the second martensite variant can be expected at least at a strain level of about 3%.

During compressive deformation up to 10.7% strain at room temperature, the initial Co–Ni–Ga single crystal runs through three different regimes of elastic or pseudoelastic deformation, respectively (Fig. 2j). These are region I = elastic deformation of austenite, region II = phase transformation stress plateau and region III = elastic deformation of martensite. Region III starts at about 4.6% macroscopic strain and continues up to the maximum load applied resulting in 10.7% strain. Since an elastic deformation of about 6% is quite unusual for metallic alloys, the microstructural mechanisms accountable for the enormous elastic deformation of the martensite need to be analyzed in detail. Furthermore, the formation of a small hysteresis upon unloading in region III at the first glance indicates that the deformation of martensite in region III is not solely elastic, i.e., there is a small non-elastic contribution. Thus, the following potential non-elastic mechanisms during deformation in region III need to be evaluated in light of the evolving stress hysteresis: (i) detwinning and

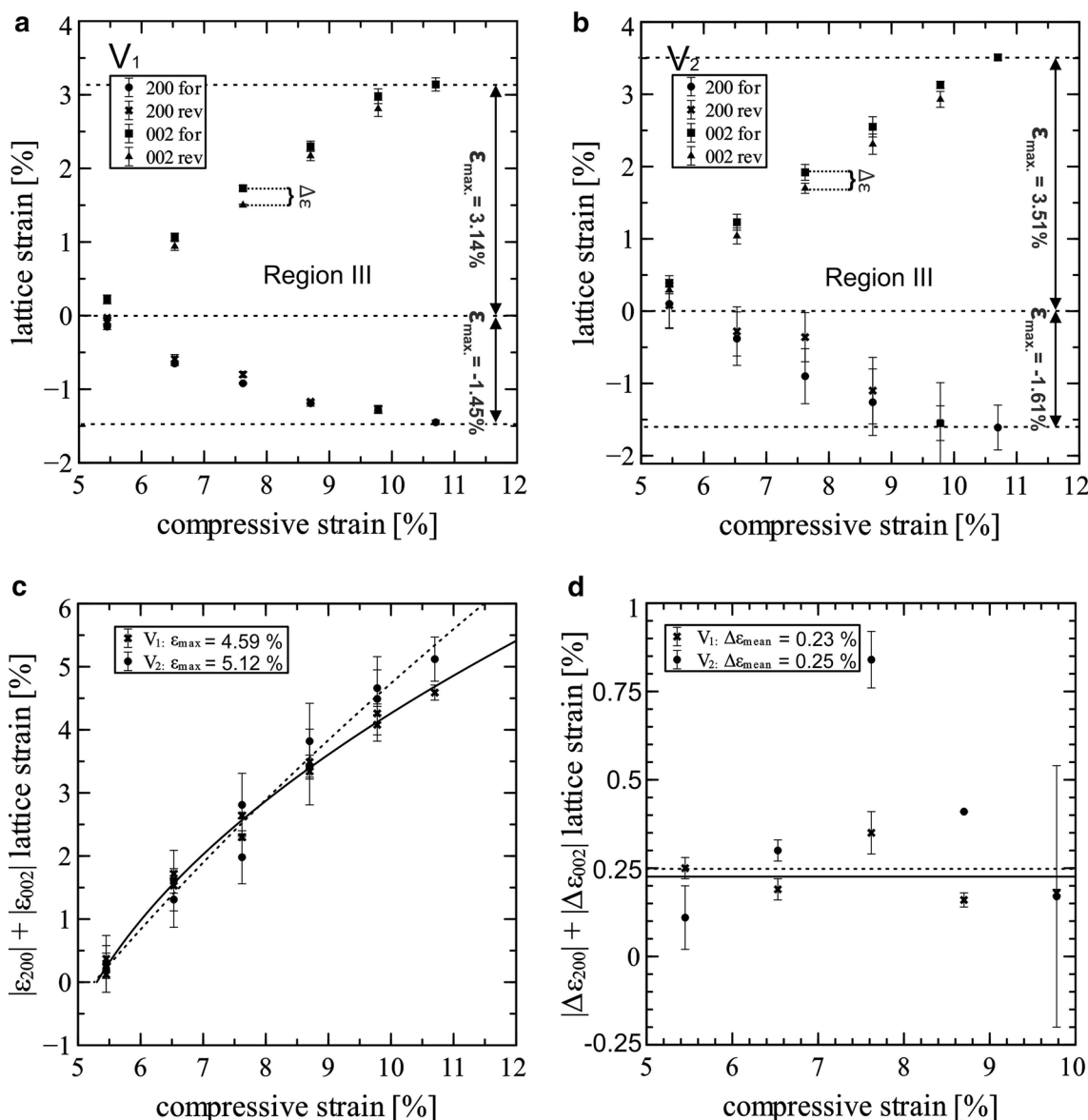


Fig. 5 **a, b** Lattice strain evolution of V_1 and V_2 transverse to the load axis for each loading stage, **c** stress-induced elastic lattice strain is non-linear and reaches 5%, while **d** the hysteretic offset is 0.25% strain on average

concomitant phase/twin boundary friction, (ii) plastic deformation of the sample perpendicular to the loading axis, (iii) interaction/friction between the sample and the grips.

The hysteretic stress–strain response could be rationalized by the occurrence of detwinning, due to frictional energies at variant–variant boundaries [27, 28]. However, in the elastic martensite region, the volume ratio of both martensite domain variants remains nearly constant (Fig. 4). Hence, detwinning can be excluded as a potential explanation for the small stress–strain hysteresis seen. Plastic deformation of the material can be excluded as well, as the original austenite state is fully recoverable without residual strains (Fig. 2j, red dot highlighted “h”).

The lattice strain evolution along the c -axis (as measured by the lattice spacing $d_{(002)}$) and a -axis (as measured by $d_{(200)}$) of both martensite domain variants, and normalized with respect to the corresponding d -spacings of martensite at the end of the plateau for each loading stage in the elastic martensite region is summarized in Fig. 5a, b. According to the diffraction geometry used, lattice strains were only measured transverse to the load axis. The elastic lattice strain for both crystallographic directions is distinctly non-linear; it is positive in c -direction and negative in a -direction, where the c -axis strain is consistently about twice as high as the absolute value of the a -axis strain. Note that the compression of the a -direction is not measured parallel to the compressive load axis, but

perpendicular to it. Martensite domain variant V_1 exhibits a maximum elastic lattice strain of 3.14 and -1.45% along the c and a -axis, respectively. Martensite domain variant V_2 follows a very similar trend. The 2:–1 ratio of stress-induced elastic lattice strains along the c -axis and a -axis, respectively, reflects the ferroelastic order parameter of tetragonal Co–Ni–Ga. The spontaneous strain of the austenite to martensite transition displays the 2:–1 ratio such that the volume strain of the martensitic phase transition is zero, an important prerequisite for shape memory behavior [27]. Moreover, the non-linearity of the stress–strain response in region III further reflects this order parameter [29] (Fig. 5c). The total lattice strain of both martensite variants for each loading stage in region III is summarized in Fig. 5c revealing 4.59% (V_1) and 5.12% (V_2) at maximum applied stress.

The unloading curve in region III reveals a small, but quantifiable stress–strain hysteresis for both martensite variants (Fig. 5a, b). The resulting lattice strain difference between loading and unloading is denoted as $\Delta\varepsilon$ and plotted in Fig. 5d. The hysteretic offset in lattice strain of V_1 and V_2 for any given macroscopic strain (as set in strain-controlled operation mode of the testing apparatus) is fairly constant at 0.23 and 0.25% (Fig. 5d), while the elastic strain in region III, i.e., for martensite, is in the order of 5% for the maximum applied load (Fig. 5c). As detailed before, detwinning in the part of the specimen being probed by the neutron beam can be excluded just like presence of a new, alternative twinning modes. Thus, it is assumed that the small observed stress–strain hysteresis in region III is induced by self-accommodation in relation to the friction of the specimen in contact with the piston surfaces. This friction will prevent free lateral (transverse) deformation and pose local boundary conditions to austenite/martensite/twin self-accommodation, which are different from the central, bulk part of the sample, where transverse deformation is rather free to occur. As the neutron beam is confined to avoid irradiation of the stress pistons, any processes occurring at the piston/sample interface are not visible directly in the diffractograms, but they would be visible in the observed stress–strain behavior.

Consequently, none deteriorating elementary deformation mechanism seems to be activated at highest level loading of the stress-induced martensite in [001]-oriented Co–Ni–Ga HT-SMA. This will open up new possibilities for use of Co–Ni–Ga in high-strain applications. However, further studies focusing on role of temperature and cyclic stability will have to be conducted in future.

Conclusion

$\text{Co}_{49}\text{Ni}_{21}\text{Ga}_{30}$ single crystals display elastically recoverable strains up to the order of $\sim 11\%$ in compression along a cubic $\langle 001 \rangle$ -direction. This recoverable strain includes

both martensitic phase transition and elasticity of martensite. The absence of a suitable slip system seems to promote this excellent behavior.

Acknowledgements Financial support by the Deutsche Forschungsgemeinschaft (DFG) within the Research Unit Program “Hochtemperatur-Formgedächtnislegierungen” (Contract Nos. NI1327/3-2; SCHM 930/13-2) is gratefully acknowledged. Y.I.C. acknowledges the support from Russian Ministry of Education and Science (Project 16.6554.2017/6.7) and from The Tomsk State University Academic D.I. Fund Program (Project 8.140.2017).

References

- Otsuka K, Wayman CM (1999) Shape memory materials. Cambridge University Press, Cambridge
- Lagoudas DC (2008) Shape memory alloys: modeling and engineering applications. Springer, New York
- Sehitoglu H, Patriarca L, Wu Y (2017) Shape memory strains and temperatures in the extreme. *Curr Opin Solid State Mater Sci* 21:113–120
- Ma J, Karaman I, Noebe RD (2010) High temperature shape memory alloys. *Int Mater Rev* 55:257–315
- Otsuka K, Ren X (2005) Physical metallurgy of Ti–Ni-based shape memory alloys. *Prog Mater Sci* 50:511–678. <https://doi.org/10.1016/j.pmatsci.2004.10.001>
- Firstov G, Van Humbeeck J, Koval Y (2004) High-temperature shape memory alloys. *Mater Sci Eng A* 378:2–10. <https://doi.org/10.1016/j.msea.2003.10.324>
- Karakoc O, Hayrettin C, Bass M et al (2017) Effects of upper cycle temperature on the actuation fatigue response of NiTiHf high temperature shape memory alloys. *Acta Mater* 138:185–197. <https://doi.org/10.1016/j.actamat.2017.07.035>
- Saghayan SM, Karaca HE, Tobe H et al (2017) High strength NiTiHf shape memory alloys with tailorable properties. *Acta Mater* 134:211–220. <https://doi.org/10.1016/j.actamat.2017.05.065>
- Oikawa K, Ota T, Gejima F, Ohmori T, Kainuma R, Ishida K (2001) Phase equilibria and phase transformations in new B2-type ferromagnetic shape memory alloys of Co–Ni–Ga and Co–Ni–Al systems. *Mater Trans* 42:2472–2475
- Vollmer M, Krooß P, Segel C et al (2015) Damage evolution in pseudoelastic polycrystalline Co–Ni–Ga high-temperature shape memory alloys. *J Alloys Compd* 633:288–295. <https://doi.org/10.1016/j.jallcom.2015.01.282>
- Krooß P, Kadletz PM, Somsen C et al (2016) Cyclic degradation of $\text{Co}_{49}\text{Ni}_{21}\text{Ga}_{30}$ high-temperature shape memory alloy: on the roles of dislocation activity and chemical order. *Shape Mem Superelast* 2:37–49. <https://doi.org/10.1007/s40830-015-0049-5>
- Dadda J, Maier HJJ, Karaman I et al (2006) Pseudoelasticity at elevated temperatures in [001] oriented $\text{Co}_{49}\text{Ni}_{21}\text{Ga}_{30}$ single crystals under compression. *Scr Mater* 55:663–666. <https://doi.org/10.1016/j.scriptamat.2006.07.005>
- Dadda J, Maier HJ, Karaman I, Chumlyakov Y (2010) High-temperature in situ microscopy during stress-induced phase transformations in $\text{Co}_{49}\text{Ni}_{21}\text{Ga}_{30}$ shape memory alloy single crystals. *Int J Mater Res* 101:1503–1513
- Ren X, Otsuka K (1997) Origin of rubber-like behaviour in metal alloys. *Nature* 389:579–582. <https://doi.org/10.1038/39277>
- Otsuka K, Ren XB (2001) Mechanism of martensite aging effects and new aspects. *Mater Sci Eng A* 312:207–218. [https://doi.org/10.1016/s0921-5093\(00\)01877-3](https://doi.org/10.1016/s0921-5093(00)01877-3)

16. Chernenko VA, Pons J, Cesari E, Zasimchuk IK (2004) Transformation behaviour and martensite stabilization in the ferromagnetic Co-Ni-Ga Heusler alloy. *Scr Mater* 50:225–229. <https://doi.org/10.1016/j.scriptamat.2003.09.024>
17. Niendorf T, Krooß P, Somsen C et al (2015) Martensite aging—avenue to new high temperature shape memory alloys. *Acta Mater* 89:298–304. <https://doi.org/10.1016/j.actamat.2015.01.042>
18. Krooß P, Niendorf T, Kadletz PM et al (2015) Functional fatigue and tension-compression asymmetry in [001]-oriented $\text{Co}_{49}\text{Ni}_{21}\text{Ga}_{30}$ high-temperature shape memory alloy single crystals. *Shape Mem Superelast* 1:6–17. <https://doi.org/10.1007/s40830-015-0003-6>
19. Kustov S, Pons J, Cesari E, Van Humbeeck J (2004) Pinning-induced stabilization of martensite Part II. Kinetic stabilization in Cu-Zn-Al alloy due to pinning of moving interfaces. *Acta Mater* 52:3083–3096. <https://doi.org/10.1016/j.actamat.2004.03.010>
20. Dadda J, Maier HJ, Niklasch D et al (2008) Pseudoelasticity and cyclic stability in $\text{Co}_{49}\text{Ni}_{21}\text{Ga}_{30}$ shape-memory alloy single crystals at ambient temperature. *Metall Mater Trans A* 39:2026–2039. <https://doi.org/10.1007/s11661-008-9543-0>
21. Monroe JA, Karaman I, Karaca HE et al (2010) High-temperature superelasticity and competing microstructural mechanisms in $\text{Co}_{49}\text{Ni}_{21}\text{Ga}_{30}$ shape memory alloy single crystals under tension. *Scr Mater* 62:368–371. <https://doi.org/10.1016/j.scriptamat.2009.11.006>
22. Molnár P, Šittner P, Novák V, Lukáš P (2008) Twinning processes in Cu-Al-Ni martensite single crystals investigated by neutron single crystal diffraction method. *Mater Sci Eng A* 481–482:513–517. <https://doi.org/10.1016/j.msea.2007.01.189>
23. Kadletz PM, Krooß P, Chumlyakov YI et al (2015) Martensite stabilization in shape memory alloys—experimental evidence for short-range ordering. *Mater Lett* 159:16–19. <https://doi.org/10.1016/j.matlet.2015.06.048>
24. Kannarpady GK, Bhattacharyya A, Wolverson M et al (2008) Phase quantification during pseudoelastic cycling of Cu-13.1Al-4.0Ni (wt%) single-crystal shape memory alloys using neutron diffraction. *Acta Mater* 56:4724–4738. <https://doi.org/10.1016/j.actamat.2008.05.028>
25. Stebner AP, Vogel SC, Noebe RD et al (2013) Micromechanical quantification of elastic, twinning, and slip strain partitioning exhibited by polycrystalline, monoclinic nickel-titanium during large uniaxial deformations measured via in situ neutron diffraction. *J Mech Phys Solids* 61:2302–2330. <https://doi.org/10.1016/j.jmps.2013.05.008>
26. Keen DA, Gutmann MJ, Wilson CC (2006) SXD—the single-crystal diffractometer at the ISIS spallation neutron source. *J Appl Crystallogr* 39:714–722. <https://doi.org/10.1107/S0021889806025921>
27. Bhattacharya K (2003) *Microstructure of martensite: why it forms and how it gives rise to the shape-memory effect*. Oxford University Press, Oxford
28. Laplanche G, Birk T, Schneider S, Frenzel J, Eggeler G (2017) Effect of temperature and texture on the reorientation of martensite variants in NiTi shape memory alloys. *Acta Mater* 127:143–152
29. Khalil-Allafi J, Schmahl WW, Reinecke T (2005) Order parameter evolution and Landau free energy coefficients for the B2 ↔ R-phase transition in a NiTi shape memory alloy. *Smart Mater Struct* 14:192–196. <https://doi.org/10.1088/0964-1726/14/5/003>